


Recoil frequency measurement with ppb-level uncertainty by ${}^6\text{Li}$ atom interferometerYang Rui,¹ Liang Zhang,¹ Rui Li,¹ Xuemei Liu[✉],¹ Chunyang Duan,¹ Pengyue Liu,¹ Yuelong Wu,^{1,*} and Haibin Wu^{1,2,3,†}¹State Key Laboratory of Precision Spectroscopy, Institute of Quantum Science and Precision Measurement, East China Normal University, Shanghai 200062, China²Collaborative Innovation Center of Extreme Optics, Shanxi University, Taiyuan 030006, China³Shanghai Research Center for Quantum Sciences, Shanghai 201315, China (Received 19 August 2022; revised 4 February 2023; accepted 30 March 2023; published 24 April 2023)

We report a first realization of cold atom interferometers with the lightest alkali metal ${}^6\text{Li}$ atoms and precisely measure the recoil frequency. The atoms are cooled to approach the half of the photon-recoil limit by using a narrow $2S \rightarrow 3P$ ultraviolet transition. A “magic” magnetically insensitive state, a high-efficiency state preparation, and a frequency-insensitive Raman coupling are developed to overcome the challenges from the half-integer spin and hyperfine interaction of atoms. A conjugated Ramsey-Bordé interferometer with crossed Raman beams is realized with a coherence time longer than 2.3 ms. The four sets of interferometers developed using geometric relations greatly eliminate the error from the angle between Raman beams. The measured recoil frequency is $\omega_r = 2\pi \times 73\,672.789(36)$ Hz, representing the most precise measurement of the recoil frequency of ${}^6\text{Li}$ by using the atom interferometer so far. The realized ${}^6\text{Li}$ cold atom interferometer is not only an effective supplement to the existing interferometers, but also provides a good candidate in precision measurement owing to its low mass and high recoil frequency.

DOI: [10.1103/PhysRevResearch.5.023052](https://doi.org/10.1103/PhysRevResearch.5.023052)

I. INTRODUCTION

A cold atom interferometer (CAI) employing a light pulse to manipulate the matter wave has been widely studied in fundamental research such as in quantum physics, general relativity, and cosmology. Owing to the ultraprecise sensing in metrology, it has become one of the most important playgrounds for precisely measuring atomic properties [1], the gravitational constant [2–5], the rotation of the earth [6], and testing fundamental physics [7,8]. Typically most CAIs utilize relatively heavy alkali atoms, such as Na, K, Rb, and Cs. For lighter lithium atoms, there are many advantages to CAI due to its low mass and high recoil velocity. For example, ${}^6\text{Li}$ and its isotope of ${}^7\text{Li}$ have a big relative weight difference and been proposed to test the standard models by measuring Einstein’s equivalence principle (EEP) with higher precision than other alkali metals [9–11]. However, due to the unresolved D_2 lines, it is difficult to cool a ${}^6\text{Li}$ atom to a very low temperature with laser cooling and thus hard to realize a cold lithium interferometer with high accuracy. Until recently, the recoil-sensitive interferometer with “warm” ${}^7\text{Li}$ atoms has been realized by using the fast Raman transitions to address the ensemble’s large Doppler spread [12]. However, to realize ${}^6\text{Li}$ CAI is still challenging. In addition to more difficult

cooling compared to ${}^7\text{Li}$, the hyperfine structure with the half-integer of the total angular momentum of ${}^6\text{Li}$ precludes the existence of a magnetically insensitive $|m_F = 0\rangle$ state. Also, small fine-structure energy splitting and much weaker coupling between the electronic and nuclear spins in ${}^6\text{Li}$ cause the small ratio of a two-photon Raman Rabi rate to an inelastic scattering rate, which further makes it difficult to realize the CAI of ${}^6\text{Li}$ [13].

Here we report a realization of the first cold ${}^6\text{Li}$ atom interferometer. Key techniques are developed to overcome the challenges to improving the precision of the CAI. Ultraviolet magneto-optical trapping (UV MOT) is implemented by using the narrow line transition $2S \rightarrow 3P$ to cool the sample below the Doppler cooling limit and approach the half of the photon-recoil limit. Magnetically insensitive Raman states and highly efficient state preparation are realized in such half-integer spin atoms. With frequency detuning insensitive Raman beams, a conjugated Ramsey-Bordé interferometer of cold ${}^6\text{Li}$ atoms exceeding 2.3 ms coherence time is realized. Using four different configurations of the interferometers, the angle of crossed Raman beams is precisely determined and the measurement accuracy is greatly improved. The measured recoil frequency is $\omega_r/2\pi = 73\,672.789(36)$ Hz, about two orders of magnitude of the uncertainty smaller one of Ref. [12], representing the currently most precise measurement of the recoil frequency of ${}^6\text{Li}$ by using the atom interferometer.

II. EXPERIMENTAL SETUP

The schematic of the experimental setup is shown in Fig. 1. The method of precooled ${}^6\text{Li}$ atoms is similar to our previous work [14–16] except that a glass ultrahigh vacuum chamber is used here. ${}^6\text{Li}$ is first cooled to about 300 μK from 673 K with

*ylwu@lps.ecnu.edu.cn

†hbwu@phy.ecnu.edu.cn

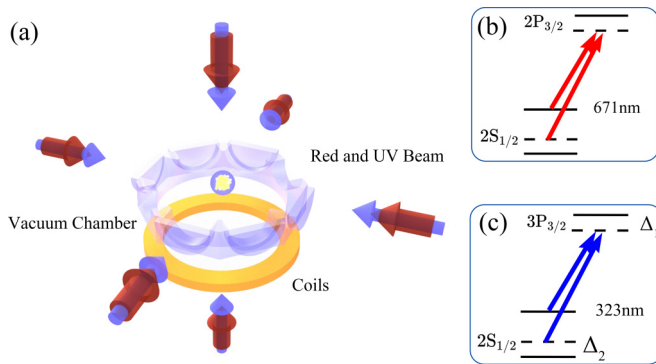


FIG. 1. Schematic of the experimental setup and the MOTs. (a) Schematic of the red MOT and UV MOT. Red (UV) MOT consists of three pairs of laser lights at 671 nm (323 nm). (b) Energy levels of red MOT; the laser lights drive the transition of $2S_{1/2} \rightarrow 2P_{3/2}$. (c) Energy levels of UV MOT; the laser lights drive the transition of $2S_{1/2} \rightarrow 3P_{3/2}$. Δ_1 is the frequency detuning between the UV MOT cooling beams and the transition of $2S_{1/2} \rightarrow 3P_{3/2}$, and Δ_2 is the frequency detuning of UV MOT cooling beams and repumping beams.

1.2×10^8 atom numbers by using a Zeeman slower and the standard MOT technique with laser of 671 nm on the transition of $2S_{1/2} \rightarrow 2P_{3/2}$. Subsequently, the atoms are transferred to a 323-nm UV MOT, which involves a narrow-line cooling of $2S_{1/2} \rightarrow 3P_{3/2}$ transition with a natural linewidth $\Gamma = 2\pi \times 754$ kHz (the Doppler cooling limit $T_D = 18 \mu\text{K}$). The UV laser is achieved by a fourth harmonic generation with a 1293-nm seed laser locked to an optical frequency comb and an ultrastable cavity (see Appendix A). For the $2S \rightarrow 3P$ UV transition, the single-photon-recoil frequency shift ω_R is comparable to Γ , and thus directly influences the thermodynamic trap properties of MOT [17,18]. When $s = I/I_s$ approaches unity, where I is the intensity of the cooling beams and I_s is the saturation intensity of the transition, the photon-recoil-driven impulsive force dominates at small frequency detunings of the cooling beams, and the temperature can be cooled to fall below the photon-recoil limit ($T_R = 2\hbar\omega_R/k_B = 30.4 \mu\text{K}$, where k_B is Boltzmann's constant) as predicted by a fully quantum treatment [17,19,20]. The temperature and atom number as a function of the frequency detuning Δ_1 between the UV MOT cooling beams and the transition of $2S_{1/2} \rightarrow 3P_{3/2}$ at fixed frequency detunings Δ_2 of UV MOT cooling beams and repumping beams are displayed in Fig. 2. As is shown, it is clear that the temperature of the atoms becomes colder as Δ_1 is decreased [Fig. 2(a)]. For very small s [red dots in Fig. 2(a)], the temperature is cooled to be smaller than the Doppler cooling limit T_D . As Δ_1 further decreases, the temperature is cooled to approach the half of the photon-recoil limit T_R . To our knowledge, this is the first realization of cooling the temperature of ${}^6\text{Li}$ to near $T_R/2$ in the MOT. There is an optimal Δ_1 for the available maximized atom number [Fig. 2(b)]. Therefore, we first load atoms into UV MOT at $\Delta_1 \approx 3\Gamma$, then a cooling phase follows, where Δ_1 is linearly decreased to 1.0Γ within 15 ms to reduce the temperature of the cloud. The loading efficiency from red MOT to UV MOT is about 50%, thus 6×10^7 atoms are obtained at the temperature of $40 \mu\text{K}$. It is essential to prepare the atomic

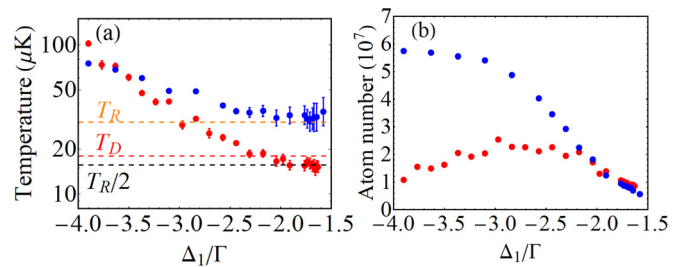


FIG. 2. (a) Temperature and (b) atom number of the cloud as a function of the dimensionless frequency detuning Δ_1/Γ with the detuning $\Delta_2/\Gamma = -0.4$. The red and black dashed lines denote the Doppler cooling limit $T_D = 18 \mu\text{K}$ and half of the photon-recoil cooling limit T_R , respectively. Red and blue dots correspond to the single-cooling (repumping)-beam peak intensity of $0.04 I_s$ ($0.02 I_s$) and $0.7 I_s$ ($0.35 I_s$), respectively, where $I_s = 13.8 \text{ mW/cm}^2$ is the saturation intensity for the transition. As Δ_1/Γ decreases, the atoms become colder. There is an optimum for the dependence of the atom number on Δ_1/Γ .

ensemble to a single magnetic sublevel for the CAIs [21,22]. For ${}^6\text{Li}$, the states labeled by $|i\rangle$ ($i = 1, 2, \dots, 6$) in order of increasing energy in a magnetic field are the six ground-state hyperfine states. Two-photon Raman transition can occur between states with $\Delta m_F = 0, \pm 1$. The atoms have to initially prepare on either the $|1\rangle$ or $|2\rangle$ state to get the high contrast to the interferometers. Usually, such a state preparation (SP) is realized by only using an optical pumping field [23–25] or an rf field [26,27]. However, the total atomic angular momentum of ${}^6\text{Li}$ is a half-integer, and no $|m_F = 0\rangle$ state is available as a dark state for efficient optical pumping. A pumping configuration of combining both 323-nm UV optical and rf fields is simultaneously applied in the experiment, as shown in Fig. 3(a). After the UV MOT, the populations of the atoms are almost equally distributed on the states of $|1\rangle$ and $|2\rangle$ [see the inset of Fig. 3(b)]. Then, the repumping beams of the UV MOT are turned off and the cooling beams of the UV MOT are kept on. An rf field with a frequency of 228.475 MHz is used to couple states $|1\rangle \rightarrow |6\rangle$. After the 1-ms (1.2-ms) duration of

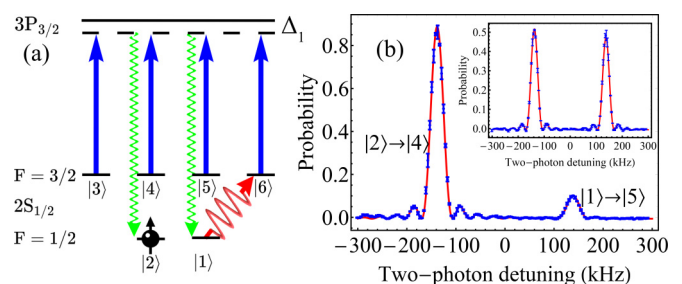


FIG. 3. The state preparation. (a) Energy levels and a pumping configuration with a 323-nm optical pumping field and an rf field. The red curved arrow represents the rf coupling of states $|1\rangle \rightarrow |6\rangle$, the blue arrows denote the 323-nm pumping fields, and the dashed green curved arrows are the spontaneous radiations in the excited states. (b) Normalized two-photon Raman spectroscopy for the SP with pumping of both rf field and UV pumping field. Inset is Raman spectroscopy without pumping fields, which shows the populations are initially equally distributed on the states of $|1\rangle$ and $|2\rangle$.

the rf field (UV light field), 90% of the total atoms are selected to be prepared in state $|2\rangle$ [Fig. 3(b)].

Another challenge from the half-integer spin of ${}^6\text{Li}$ is that it generally has no magnetic-insensitive transition of the $|m_F = 0\rangle \rightarrow |m_{F'} = 0\rangle$ to eliminate the first-order Zeeman and magnetic interaction shift. Considering the Zeeman and hyperfine interaction, the frequency shift of the Raman transitions between the ground states at the presence of the weak magnetic field B is $\delta_{m_f, m_i}^B = \frac{2}{3} \frac{\mu_B B}{h} (m_f + m_i)$, where μ_B is the Bohr magneton, h is the Planck constant, $m_f = \{-3/2, -1/2, 1/2, 3/2\}$, and $m_i = \{-1/2, 1/2\}$, respectively. For the targeted Raman transition $|2\rangle \rightarrow |5\rangle$, where $m_i = -1/2$ and $m_f = 1/2$, the frequency shift at the first-order magnetic field is zero. In a deeper level, by diagonalizing the Hamiltonian, we found that there is a “magic” magnetic field at $B_0 = 20.47$ mG, at which the energy shift E_{25} of the transition of $|2\rangle \rightarrow |5\rangle$ is insensitive to the change of the magnetic field B , i.e., $\frac{dE_{25}}{dB}|_{B=B_0} = 0$ for all orders of B . For comparison, the derivation of the energy of the magnetic-insensitive transition $|m_F = 0\rangle \rightarrow |m_{F'} = 0\rangle$ from the weak field in the other alkali metals is given by

$$\frac{dE_{00}}{dB} = \frac{(g_J - g_I)^2 \mu_B^2}{h \Delta E_{hfs}} B, \quad (1)$$

where ΔE_{hfs} is the hyperfine splitting of the ground states. The shift cannot be zero for the nonzero magnetic field B . In the experiment, in order to avoid a small amount of hysteresis in other metal parts of the vacuum system, $B = 150$ mG along the y axis is used to define the quantum axis. Under this magnetic field, the energy shift and its change rate of the transition are about 250 Hz and 40 mHz for the 10- μG variation of the magnetic field, which is comparable to the magnetic-insensitive transition of other alkali metals.

III. EXPERIMENT RESULTS AND DISCUSSION

A ${}^6\text{Li}$ interferometer is realized by using a conjugated Ramsey-Bordé interferometer [23–25] which consists of a sequence of four $\pi/2$ stimulated Raman pulses to split, redirect, and interfere with the atomic matter waves, as shown in Fig. 4. The intensity and diameter of each Raman beam are 300 mW and 4.3 mm, respectively. For the atom interferometer, it is essential to precisely determine the effective Rabi frequency of Raman beams. For ${}^6\text{Li}$, due to the smaller hyperfine splitting compared to other alkali atoms, all transitions of D_1 and D_2 lines have to be taken into account. We measured the effective Rabi frequency as a function of single-photon detunings, and found that the change of the effective Rabi frequency is insensitive to the frequency detunings when the single-photon detuning is around 5 GHz (see Appendix B). Therefore, the frequency of Raman beams is fixed to this frequency, and the effective Rabi frequency is $2\pi \times 0.96$ MHz. The corresponding duration of $\pi/2$ pulses is about 280 ns, which covers most of the velocity distribution of the cold atoms. A pair of Raman beams propagated perpendicularly to each other is used to realize the atom interferometer. First, a σ^+ polarized Raman beam 1 (RB1) and a π polarized Raman beam 2 (RB2) are turned on at the same time. The atoms in state $|2\rangle$ obtain an effective momentum $\hbar \vec{k}_{\text{eff}}$. After the duration of T , the second $\pi/2$ pulse is turned on to split the atoms.

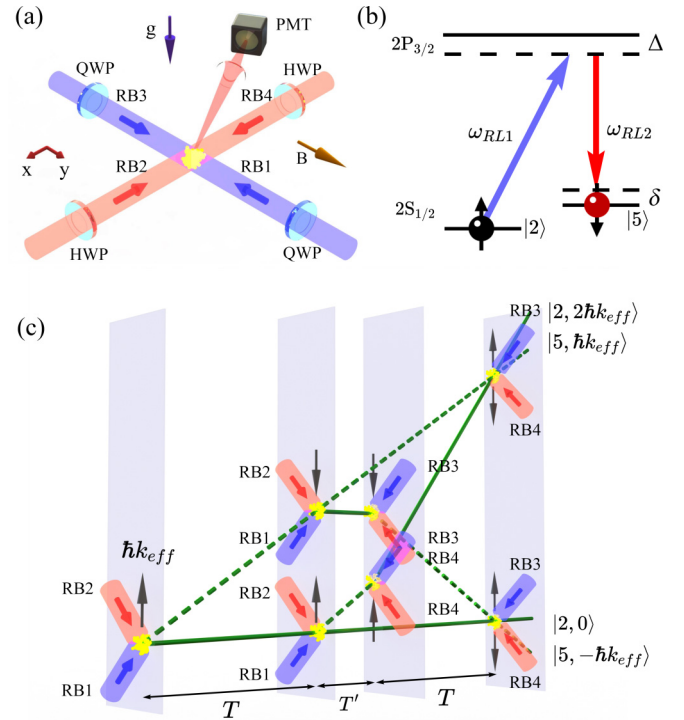


FIG. 4. A conjugated Ramsey-Bordé interferometer of ${}^6\text{Li}$. (a) The crossed Raman beams. RB1, RB2, RB3, and RB4 are the four Raman beams. HWP and QWP are the half-wave plate and quarter-wave plate, respectively. PMT is the photomultiplier tube. (b) Energy levels and frequencies involved in Raman transitions. The configuration of $\sigma^+ - \pi$ polarized Raman beams are used to address Raman states $|2\rangle$ and $|5\rangle$. Δ and δ are the single-photon detuning and two-photon detuning, respectively. (c) Space-time trajectories of atoms in Ramsey-Bordé interferometers. A sequence of four $\pi/2$ stimulated Raman pulses coherently addresses the $|2\rangle$ state of the atoms and provides the state-dependent momentum kicks, where $k_{\text{eff}} = \sqrt{2}k$.

After these two $\pi/2$ pulses waited for a duration of T' , Raman beams 3 and 4 (RB3 and RB4) with a time interval of T are turned on with reversing effective wave vectors to complete the interferometer. Because the high-bandwidth pulses used to interact with a broad velocity class simultaneously address both transitions, two interferometers' output ports overlap spatially since the samples thermally expand faster than the interferometers separation. The atoms initially prepared in state $|2\rangle$, after a sequence of Raman pulses, appear in state $|5\rangle$ with a possibility [12]

$$P_5 = D \{ 1 - e^{-t/\tau} [C_1 \cos(\Delta\phi^+) + C_2 \cos(\Delta\phi^-)] \}, \quad (2)$$

where D is a total fringe shift, τ represents the coherence time of the interferometer, and C_1 (C_2) is the contrast of upper (lower) interference fringe. The phase difference of the upper (lower) interferometer $\Delta\phi^+$ ($\Delta\phi^-$) is given by

$$\Delta\phi^\pm = \pm 4\omega_r T + 2\delta T + 2k_{\text{eff}} a_z T (T + T') + \varphi_0, \quad (3)$$

where the first term arises from the atomic kinetic energy, and ω_r is the recoil frequency [$\omega_r = \hbar k^2 / (2m)$]. The second term arises from the two-photon detuning $\delta = \omega_{RL1} - \omega_{RL2} - (\omega_2 - \omega_5)$, ω_{RL1} and ω_{RL2} are the Raman laser frequencies,

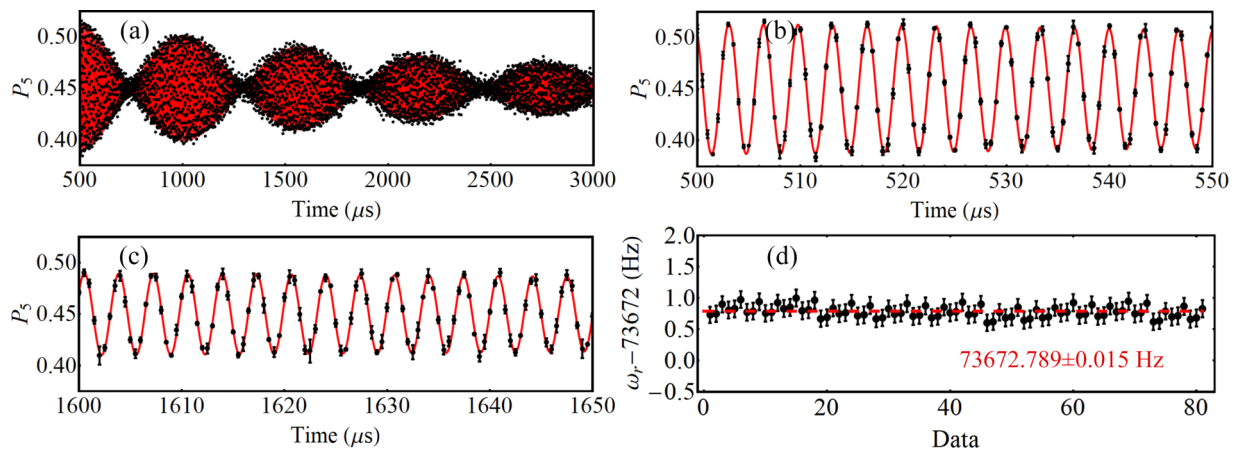


FIG. 5. Beating interference of the ${}^6\text{Li}$ atom interferometer. (a) The probability P_5 of detecting atoms in the $|5\rangle$ state oscillates due to the detuning of $\delta = 2\pi \times 489$ Hz. Each point is the average of three experimental shots with the same experimental parameters. (b and c) Closer inspection of the fringe at evolution periods of $T \approx 500\text{--}550$ μs and $T \approx 1600\text{--}1650$ μs , respectively. (d) The measured recoil frequencies from the four atom interferometers. The error bar is from statistics.

and $\omega_2 - \omega_5$ is the resonance frequency between states $|2\rangle$ and $|5\rangle$. The third term is from the acceleration a_z along the direction of the effective wave vector. The fourth term is the phase difference at the initial time.

After the sequence of the interferometer with four $\pi/2$ pulses, a detection of atoms in state $|5\rangle$ is followed (see Appendix C). A probe beam detuned -20 MHz to $|2S_{1/2}, F = 3/2\rangle \rightarrow |2P_{3/2}\rangle$ is first illuminated for 30 μs . A high-gain photomultiplier tube (PMT) is used to collect fluorescence signals [28,29]. Then, a beam with the resonant frequency of the transition of $|2S_{1/2}, F = 1/2\rangle \rightarrow |2P_{3/2}\rangle$ is used to pump all the atoms to $|F = 3/2\rangle$. Subsequently, the probe beam is turned on again for 30 μs to detect the atoms in state $|5\rangle$ again. The ratio of two detected fluorescence signals gives the probability of atoms in state $|5\rangle$ with suppressing the shot-to-shot noise from the atom number fluctuation.

To precisely measure the recoil frequency with the interferometer with the crossed Raman beams, the angle between the Raman beams has to be precisely determined. In the experiment, we carefully align the beams between RB1 and RB2. RB3 and RB4 are coupled into the same fibers of outputting RB1 and RB2 to make sure that they are collinear with RB1 and RB2, respectively. However, the small deviation from the exact 90° of Raman beams can contribute to the measurement. So we develop a method to cancel the influence from the angle by realizing four sets of interferometers (see Appendix D). For four $\pi/2$ pulses, we select a pair of RB1 and RB2, RB2 and RB3, RB3 and RB4, RB4 and RB1 as the first two pulses, respectively. Other pairs of RB3 and RB4, RB4 and RB1, RB1 and RB2, RB2 and RB3 are used as the last two pulses. So there are four sets of the conjugated Ramsey-Bordé interferometers. The interference data of the first interferometer are shown in Figs. 5(a)–5(c). The measured recoil frequency and coherence time τ can be extracted from the fit with Eq. (2) (red lines). The advantage of four such interferometers is that the influence from the angle on the measurement can be greatly suppressed by averaging the four measurements (see Appendix D). Each interferometer is repeated three runs with the same parameters. We arbitrarily select measured results in the four interferometers to average and obtain 81

measurements of the recoil frequencies [Fig. 5(d)], which lead to the recoil frequency $\omega_r = 2\pi \times 73\,672.789$ (15) Hz and coherence time about $\tau = 2363$ (23) μs , respectively. Taking other uncertainties into account, the final recoil frequency is given by $\omega_r = 2\pi \times 73\,672.789$ (36) Hz.

Compared with the interferometer of ${}^7\text{Li}$ in Berkeley [12], the uncertainty of measured recoil frequency of developed ${}^6\text{Li}$ CAI is about two orders of magnitude smaller and the coherence time is about one order of magnitude longer. Using the new SI value for the Planck constant h [30], and the mass of ${}^6\text{Li}$ from the measurements of cyclotron frequency ratios of pairs of ions simultaneously trapped in a Penning trap [31], the recoil frequency is determined by $\omega_r = 2\pi \times 73\,672.764\,687$ (29) Hz. Our measurement is a mere $1\text{-}\sigma$ away from the above value, therefore representing the most precise measurement of the recoil frequency of ${}^6\text{Li}$ by using the CAI so far.

Here the uncertainty is mainly limited by the interference time and a 4.4-ms lifetime of the cold atom. A Monte Carlo calculation is developed to simulate this limitation. The coherence time of the interference signal at 40 μK is nearly three times longer than one at 300 μK . The relative uncertainty budgets for the measurement, such as the influence of the magnetic field, the power and frequency stability of Raman beams, and the AC Stark effect, are shown in Table I.

TABLE I. Relative uncertainty budgets for the measurement.

Uncertainty component	Shift	Variance
Magnetic field		3.5×10^{-7}
Phase fluctuation of fibers		5.6×10^{-8}
Single-photon detuning		6.3×10^{-9}
Coriolis force		$<1 \times 10^{-8}$
Wavefront curvature	-3.5×10^{-9}	
AC Stark		2.8×10^{-7}
Systematic uncertainty	-3.5×10^{-9}	4.5×10^{-7}
Statistical uncertainty		2.0×10^{-7}
Total	-3.5×10^{-9}	4.9×10^{-7}

The insensitivity of the Raman transition of $|2\rangle \rightarrow |5\rangle$ to the magnetic field is crucial to get the high-contrast atom interferometer. We have developed the ${}^6\text{Li}$ atom interferometer with the same conditions for the Raman states $|2\rangle \rightarrow |4\rangle$, for which the coherent time is reduced to 0.5 ms, which is almost four times shorter than one with a Raman transition of $|2\rangle \rightarrow |5\rangle$. Another factor is the AC stark effect, where atoms in different positions of Raman beams feel different intensities. With the measured power spectrum of the intensity noises of the Raman beams, the relative uncertainty from the variation of the beam intensity is less than 2.8×10^{-7} by the developed Monte Carlo simulation. As pointed out in Ref. [12], the common-mode noises of vibration-induced signals are greatly suppressed. One of the big uncertainties is from the intensity fluctuations of Raman beams between the different experimental runs due to the polarization jitter of long fibers. The limitation to achieve the so-called shot-noise-limited sensitivity is mainly from the fluorescence detection efficiency and the lifetime of the excited states, which cause one order of magnitude of the detection noise higher than the atom shot noise.

IV. CONCLUSION

In conclusion, we have realized the first ${}^6\text{Li}$ atom interferometer and precisely measured its recoil frequency. An ${}^6\text{Li}$ atom is cooled to lower than the recoil temperature by using the narrow line cooling method. Combined with the magnetic-insensitive configuration and the efficient state preparation, the uncertainty of the measured recoil frequency reaches a precision of 490 ppb. The realized ${}^6\text{Li}$ interferometer is not only a supplement to the existing atom interferometers, but also potentially provides a new avenue in metrology owing to its low mass and high recoil frequency. For example, if combined with the large momentum transfer technique of 500 photons, the current ${}^6\text{Li}$ interferometer just using $T = 30$ ms interrogation time is comparable with the state-of-the-art measurements of the fine structure constant [7,8]. We are generalizing such interferometers to cold atoms of ${}^6\text{Li}$ and ${}^7\text{Li}$, which have the potential to test the principle of equivalence at the higher precision level.

ACKNOWLEDGMENTS

This research is supported by the National Key Research and Development Program of China (Grant No. 2022YFA1404202), the National Natural Science Foundation of China (NSFC) (Grants No. 11925401, No. 11734008, No. 11374101, and No. 12074125), and the Shanghai Municipal Science and Technology Major Project (No. 2019SHZDZX01).

APPENDIX A: LOCKING OF THE UV LASER

In atom interferometers, it is very important to suppress the decoherence from atomic motion by further cooling the atoms. In ${}^6\text{Li}$, we observe a temperature near $T_R/2$ (photon-recoil limit $T_R = 2\hbar\omega_R/k_B = 30.4 \mu\text{K}$) by the narrow-line cooling of $2S \rightarrow 3P$ transition. To obtain such cold atom samples, the UV laser of 323 nm is crucial.

The frequency-stabilized 323-nm laser is generated by using two resonant doubling cavities by a 1293-nm seed laser, which is locked into the optical frequency comb (OFC). The OFC is referenced to an ultrastable optical cavity. The cavity drifts 4 kHz per day and the instability of OFC is better than 2×10^{-16} at 1-s average at 1293 nm. The linewidth of the seed laser is less than 1 Hz, resulting from locking to the OFC via a high-speed servo circuit. A pinhole spatial filter is used to improve laser quality by removing higher-order modes and noise in the beam. To obtain the ultrastable UV laser near the atomic transition of $2S_{1/2} \rightarrow 3P_{3/2}$, we built a 1.2-m-long heat pipe of ${}^6\text{Li}$ to enhance the absorption for the narrow-line transition and therefore to obtain the high-resolution saturation absorption spectroscopy. The linewidth of the seed laser is from 30 kHz to less than 1 Hz because of the replacement of the saturation absorption spectrum by OFC. Benefitting from the locking, the frequency detuning Δ_1 is precisely controlled when decreasing it to the near-resonant range in the narrow-line cooling.

APPENDIX B: INSENSITIVE SINGLE-PHOTON DETUNING OF RAMAN BEAM

The atom interferometer will be impacted seriously by $\pi/2$ pulse time, which is related to the detuning of Raman beams. We find a detuning point where the pulse time is insensitive to the fluctuation of detuning.

The effective Rabi frequency of Raman process can be written as follows:

$$\Omega_{\text{eff}} = \sum_i \frac{\Omega_{5i}\Omega_{2i}}{2\Delta_i}, \quad (\text{B1})$$

where Ω_{5i} is the Rabi frequency of the transition between state $|5\rangle$ and virtual state $|i\rangle$, Ω_{2i} is the Rabi frequency of the transition between states $|2\rangle$ and $|i\rangle$, and Δ_i is single-photon detuning between laser frequency ω_{RL1} and the frequency of the transition between states $|2\rangle$ and $|i\rangle$.

We measured the effective Rabi frequency under different single-photon detunings, and the results are shown in Fig. 6. f_{D_1} is the transition frequency of $|2S_{1/2}, F = 1/2\rangle \rightarrow |2P_{1/2}, F = 3/2\rangle$ (446 789 757 MHz). We find the so-called frequency-insensitive point where single-photon detuning is 5014 MHz. We lock the Raman laser on the crossover of the D_1 and D_2 lines through the saturated absorption spectrum by increasing the temperature of the lithium heat pipe to 400 °C. The locking accuracy is about 1.5 MHz. Then, we shift the frequency of the Raman beam by acousto-optic modulator to the frequency-insensitive point, and the effective Rabi frequency is $2\pi \times 0.96$ MHz.

APPENDIX C: DETECTION OF THE ATOM NUMBERS AND NORMALIZATION

The interference fringe of the interferometer is detected through a PMT by collecting the fluorescence of atoms. In the detection process, the atom cloud is illuminated by three orthogonal pairs of counterpropagating probe beams. The probe beam is near resonant with a cycling transition of $|F = 3/2\rangle \rightarrow |F' = 5/2\rangle$.

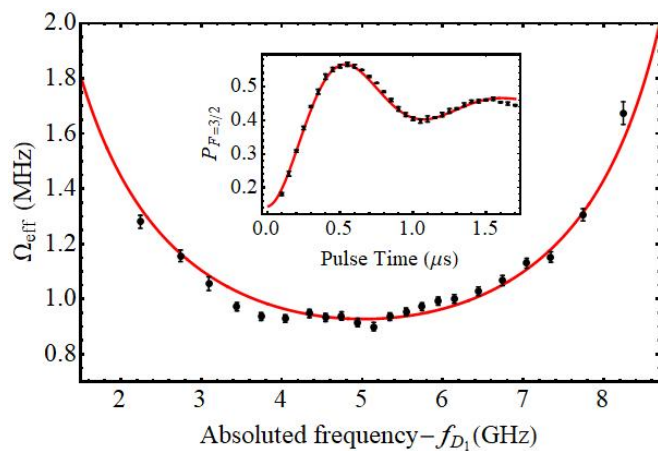


FIG. 6. The measured effective Rabi frequencies (black points) are different because of the detuning, and the theory (red solid line) is in good agreement with them. Inset: Rabi oscillation of the perpendicular Raman beams when the detuning is 5014 MHz over f_{D_1} . The black points are population of different pulse duration of Raman transition and the solid line is the damping sine fitting. The duration of $\pi/2$ pulse is insensitive to the fluctuation of the detuning in this point.

In a two-level model, the atoms in the excited state emit photons at a rate of $R_{s0} = \Gamma/2\gamma(\Delta)I/I_s$, where $\gamma(\Delta) = (1 + I/I_s + 4\Delta^2/\Gamma^2)^{-1}$ is proportional to the scattering cross sections of the detection fluorescence transition, Γ is the natural linewidth of the excited state, I_s is the saturation intensity, and Δ is the frequency detuning, respectively.

However, for ${}^6\text{Li}$, the excited states of the D_2 line are partially resolved. There are three coupled hyperfine structures: $|F' = 1/2\rangle$, $|F' = 3/2\rangle$, and $|F' = 5/2\rangle$. The near-resonant probe beam coupling $|F = 3/2\rangle \rightarrow |F' = 5/2\rangle$ induces not only the desired transition but also the $|F = 3/2\rangle \rightarrow |F' = 3/2\rangle$ and $|F = 3/2\rangle \rightarrow |F' = 1/2\rangle$ transition. A part of the atoms in these undesired excited states spontaneously decays to the $|F = 1/2\rangle$ ground state, which is decoupled from the excitation and emission cycle. For one atom, the scattered photons will be reduced with the increasing of detection time [28]

$$n_s(t) = \frac{\gamma_d}{\gamma_l} \left[1 - \exp\left(-t \frac{I}{2I_{\text{sat}}} \Gamma \gamma_l\right) \right], \quad (\text{C1})$$

where $\gamma_d = \gamma(\Delta)$, $\gamma_l = \sum_i \gamma(\Delta_i) \text{br}_i$ is proportional to the scattering cross sections of all the lost nonclosed transitions (br_i is the spontaneous emission branching ratio to nonclosed transitions). $\Delta_i = \Delta_{di} - \Delta$ is the detuning with respect to the nondetection hyperfine transitions, and Δ_{di} is the frequency difference of these transitions with respect to the detection one. In ${}^6\text{Li}$ atoms, the branch ratios of the nonclosed transition of $|F = 1/2\rangle \rightarrow |F' = 3/2\rangle$ and $|F = 1/2\rangle \rightarrow |F' = 1/2\rangle$ are 55.6% and 83.9%. With $R_s = \frac{dn_s}{dt}$, the modified scattering rate is given by

$$R_s(t) = R_{s0} \exp\left(-\frac{t}{\tau}\right), \quad (\text{C2})$$

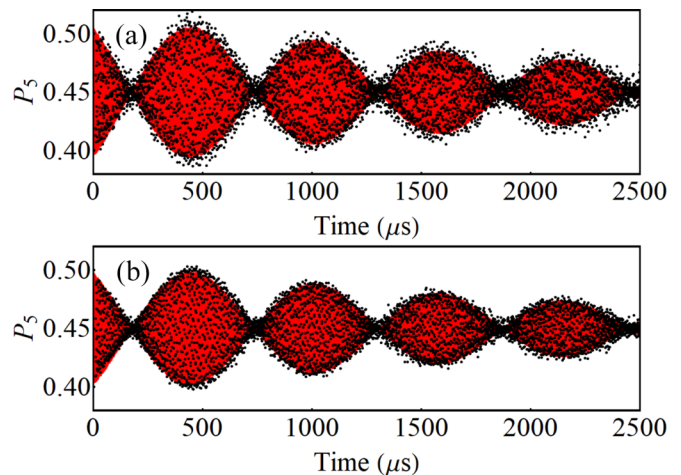


FIG. 7. Beating interference of the ${}^6\text{Li}$ atom interferometer (a) without and (b) with the atom number normalization. The black dots are measured data and the red line is a fitting curve.

where $\tau = 2/(s\Gamma\gamma_l)$ is the damping time. In the experiment, the scattering photons are collected by a lens. A voltage signal of scattering photons from the atoms is given by

$$V(t) = NR_{s0}\Omega T\eta eGR_f \exp(-t/\tau) + V_{\text{dark}}, \quad (\text{C3})$$

where Ω is a solid angle by the lens, e is the elementary charge of an electron, G is the current gain of the PMT, η is the quantum efficiency of the photodiode, R_f is the resistor in transimpedance amplifier, and V_{dark} is from the dark current of the PMT, respectively.

Although the atom number N can be determined by measuring the voltage signal $V(0)$, the limited response of the PMT inevitably leads to a uncertainty for the atom number. In order to better get the normalization of the atom number, we measure the integrated voltage signal S to determine the atom number,

$$S = \int_0^{t_d} V(t) dt = n_s(t_d)K + V_{\text{dark}}t_d, \quad (\text{C4})$$

where t_d is the measured time and $K = \Omega T\eta eGR_f$. When t_d is long enough, $n_s(t_d) \rightarrow N \frac{\gamma_d}{\gamma_l}$ and $S_{t_d \rightarrow \infty} = N\gamma_d/\gamma_l K + V_{\text{dark}}t_d$.

In the experiment, we detect the atom number in state $|5\rangle$ twice. First, after the sequence of the interferometer, a probe beam is turned on for 30 μs for measurement of the atom number in state $|5\rangle$. Subsequently, a beam with resonant frequency $|2S_{1/2}, F = 1/2\rangle \rightarrow |2P_{3/2}\rangle$ is used to pump all the atoms to $|F = 3/2\rangle$ from $|F = 1/2\rangle$. The probe beam is turned on again for 30 μs to detect the atoms in state $|5\rangle$ again. The ratio between these two measurements is given by

$$\frac{S_{1t_d \rightarrow \infty}}{S_{2t_d \rightarrow \infty}} = \frac{N_1\gamma_d/\gamma_l K + V_{\text{dark}}t_d}{N_2\gamma_d/\gamma_l K + V_{\text{dark}}t_d} \approx \frac{N_1}{N_2}. \quad (\text{C5})$$

For the large detection time and negligible dark current, the ratio of two measurements is given by N_1/N_2 , where N_1 and N_2 are the atom number in state $|5\rangle$ for two measurements, respectively.

We use this normalization to detect the probability of the atoms in state $|5\rangle$ after the interferometer. The results with and without the normalization are shown in Fig. 7. It is clear

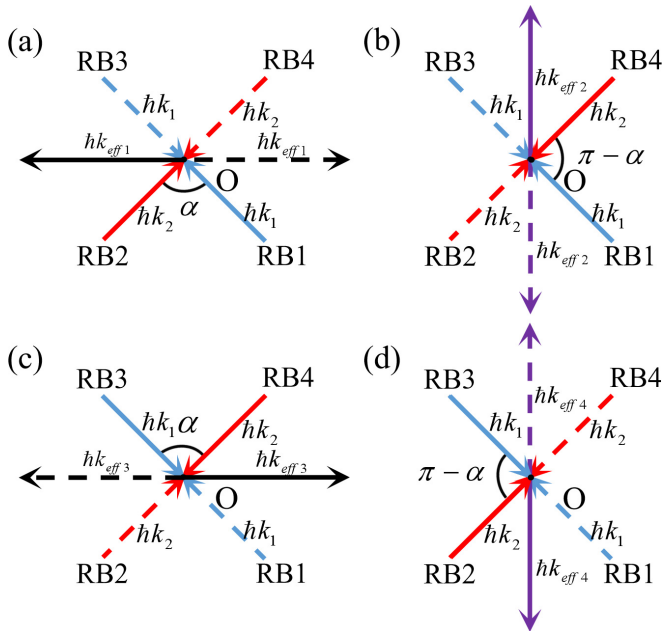


FIG. 8. The configuration of Raman beams of four sets of interferometers. (a) The first two $\pi/2$ pulses are RB1 and RB2, and their angle is α . The last two $\pi/2$ pulses are RB3 and RB4. (b) The first two $\pi/2$ pulses are RB1 and RB4. The last two $\pi/2$ pulses are RB2 and RB3. (c) The first two $\pi/2$ pulses are RB4 and RB3. The last two $\pi/2$ pulses are RB1 and RB2. (d) The first two $\pi/2$ pulses are RB2 and RB3. The last two $\pi/2$ pulses are RB1 and RB4. The atoms in state $|2\rangle$ will obtain a momentum $\hbar k_{\text{eff}1}$ ($\hbar k_{\text{eff}2}$, $\hbar k_{\text{eff}3}$, $\hbar k_{\text{eff}4}$) by stimulated Raman process with RB1 and RB2 (RB1 and RB4, RB3 and RB4, RB2 and RB3). The minor angle deviation from 90° can be corrected by averaging the results of four sets of the interferometers.

that the ratio of the signal to noise is improved, the fluctuation from the atom number is greatly suppressed, and the fitting accuracy of recoil frequency is improved about twofold by using this normalization.

APPENDIX D: PRECISE DETERMINATION OF THE ANGLE OF THE RAMAN BEAMS

The conjugate Ramsey-Bordé interferometers in the experiment are realized by four $\pi/2$ Raman beams, which are perpendicular to each other to take advantage of the magnetically insensitive state. The RB1 and RB3 are high-frequency beams and the RB2 and RB4 are low-frequency beams,

respectively. Although the counterpropagating RB1 (RB2) is collimated by coupling its beam into the optical fiber for outputting RB3 (RB4), it is difficult to achieve exact 90° between Raman beams, which could have an effect on the accuracy of the measurement of the recoil frequency. We develop the method to cancel the effect from the angle by realizing four sets of conjugate Ramsey-Bordé interferometers, as shown in Fig. 8.

In the first set of the four interferometers of Fig. 8(a), the first two $\pi/2$ pulses consist of RB1 and RB2 (solid arrows), and the atoms are transferred from state $|2\rangle$ to state $|5\rangle$ with a momentum $\hbar k_{\text{eff}1}$ (solid black arrow), where $\hbar k_{\text{eff}1}$ is the effective wave vector. The last two $\pi/2$ pulses consist of RB3 and RB4 (dashed arrows), and the atoms are transferred from state $|2\rangle$ to state $|5\rangle$ with the momentum $\hbar k_{\text{eff}1}$ (dashed black arrow) along the opposite direction of the first two $\pi/2$ pulses. Therefore, the effective wave vector can be simply obtained as

$$k_{\text{eff}1}^2 = k_1^2 + k_2^2 - 2k_1k_2 \cos \alpha. \quad (\text{D1})$$

Similarly, in Figs. 8(b)–8(d) for the different set of interferometers, the first two $\pi/2$ pulses consist of RB1 and RB4, RB3 and RB4, RB2 and RB3, respectively; and the last two $\pi/2$ pulses consist of RB2 and RB3, RB1 and RB2, RB1 and RB4, respectively. The corresponding effective wave vectors are given by

$$\begin{aligned} k_{\text{eff}2}^2 &= k_1^2 + k_2^2 - 2k_1k_2 \cos(\pi - \alpha), \\ k_{\text{eff}3}^2 &= k_1^2 + k_2^2 - 2k_1k_2 \cos(\alpha), \\ k_{\text{eff}4}^2 &= k_1^2 + k_2^2 - 2k_1k_2 \cos(\pi - \alpha). \end{aligned} \quad (\text{D2})$$

Ignoring the 228-MHz frequency difference between the Raman beams, $k_1 \approx k_2 = k$, we have

$$\begin{aligned} \omega_{\text{eff}1} &= 2(1 - \cos \alpha)\omega_r, \\ \omega_{\text{eff}2} &= 2(1 + \cos \alpha)\omega_r, \\ \omega_{\text{eff}3} &= 2(1 - \cos \alpha)\omega_r, \\ \omega_{\text{eff}4} &= 2(1 + \cos \alpha)\omega_r. \end{aligned} \quad (\text{D3})$$

If the α is the exact 90° , the four sets of interferometers should give the same recoil frequency. In the experiment we develop these four interferometers and average four measured recoil frequencies, $\omega_{\text{eff}} = (\omega_{\text{eff}1} + \omega_{\text{eff}2} + \omega_{\text{eff}3} + \omega_{\text{eff}4})/4$, which greatly cancels the effect of the angle in determining the recoil frequency.

- [1] W. F. Holmgren, M. C. Revelle, V. P. A. Lonij, and A. D. Cronin, Absolute and ratio measurements of the polarizability of Na, K, and Rb with an atom interferometer, *Phys. Rev. A* **81**, 053607 (2010).
- [2] A. Peters, K. Y. Chung, and S. Chu, High-precision gravity measurements using atom interferometry, *Metrologia* **38**, 25 (2001).
- [3] A. Sugarbaker, S. M. Dickerson, J. M. Hogan, D. M. S. Johnson, and M. A. Kasevich, Enhanced Atom Interferometer Readout through the Application of Phase Shear, *Phys. Rev. Lett.* **111**, 113002 (2013).
- [4] G. Lamporesi, A. Bertoldi, L. Cacciapuoti, M. Prevedelli, and G. M. Tino, Determination of the Newtonian Gravitational Constant Using Atom Interferometry, *Phys. Rev. Lett.* **100**, 050801 (2008).
- [5] M. Jain, G. M. Tino, L. Cacciapuoti, and G. Rosi, New apparatus design for high-precision measurement of G with atom interferometry, *Eur. Phys. J. D* **75**, 197 (2021).
- [6] T. L. Gustavson, P. Bouyer, and M. A. Kasevich, Precision Rotation Measurements with an Atom Interferometer Gyroscope, *Phys. Rev. Lett.* **78**, 2046 (1997).

- [7] R. H. Parker, C. Yu, W. Zhong, B. Estey, and H. Muller, Measurement of the fine-structure constant as a test of the Standard Model, *Science* **360**, 191 (2018).
- [8] L. Morel, Z. Yao, P. Cladé, and S. Guellati-Khelifa, Determination of the fine-structure constant with an accuracy of 81 parts per trillion, *Nature (London)* **588**, 61 (2020).
- [9] M. A. Hohensee, H. Muller, and R. B. Wiringa, Equivalence Principle and Bound Kinetic Energy, *Phys. Rev. Lett.* **111**, 151102 (2013).
- [10] S. Fray, C. A. Diez, T. W. Hansch, and M. Weitz, Atomic Interferometer with Amplitude Gratings of Light and Its Applications to Atom Based Tests of the Equivalence Principle, *Phys. Rev. Lett.* **93**, 240404 (2004).
- [11] L. Zhou, S. Long, B. Tang, X. Chen, F. Gao, W. Peng, W. Duan, J. Zhong, Z. Xiong, J. Wang, Y. Zhang, and M. Zhan, Test of Equivalence Principle at 10^{-8} Level by a Dual-Species Double-Diffraction Raman Atom Interferometer, *Phys. Rev. Lett.* **115**, 013004 (2015).
- [12] K. Cassella, E. Copenhaver, B. Estey, Y. Feng, C. Lai, and H. Muller, Recoil-Sensitive Lithium Interferometer without a Subrecoil Sample, *Phys. Rev. Lett.* **118**, 233201 (2017).
- [13] R. Wei and E. J. Mueller, Magnetic-field dependence of Raman coupling in alkali-metal atoms, *Phys. Rev. A* **87**, 042514 (2013).
- [14] S. Deng, Z.-Y. Shi, P. Diao, Q. Yu, H. Zhai, R. Qi, and H. Wu, Observation of the Efimovian expansion in scale-invariant Fermi gases, *Science* **353**, 371 (2016).
- [15] R. Li, Y. Wu, Y. Rui, B. Li, Y. Jiang, L. Ma, and H. Wu, Absolute Frequency Measurement of ${}^6\text{Li}$ D Lines with khz-Level Uncertainty, *Phys. Rev. Lett.* **124**, 063002 (2020).
- [16] R. Li, Y. Wu, Y. Rui, and H. Wu, Observation of subnatural-linewidth spectra in cold ${}^6\text{Li}$ atoms, *Phys. Rev. A* **103**, 032823 (2021).
- [17] T. H. Loftus, T. Ido, A. D. Ludlow, M. M. Boyd, and J. Ye, Narrow Line Cooling: Finite Photon Recoil Dynamics, *Phys. Rev. Lett.* **93**, 073003 (2004).
- [18] H.-Z. Chen, X.-C. Yao, Y.-P. Wu, X.-P. Liu, X.-Q. Wang, Y.-A. Chen, and J.-W. Pan, Narrow-linewidth cooling of ${}^6\text{Li}$ atoms using the 2S-3P transition, *Appl. Phys. B* **122**, 281 (2016).
- [19] Y. Castin, H. Wallis, and J. Dalibard, Limit of Doppler cooling, *J. Opt. Soc. Am. B* **6**, 2046 (1989).
- [20] H. Wallis and W. Ertmer, Broadband laser cooling on narrow transitions, *J. Opt. Soc. Am. B* **6**, 2211 (1989).
- [21] R. A. Hart, X. Xu, R. Legere, and K. Gibble, A quantum scattering interferometer, *Nature (London)* **446**, 892 (2007).
- [22] M. J. Snadden, J. M. McGuirk, P. Bouyer, K. G. Haritos, and M. A. Kasevich, Measurement of the Earth's Gravity Gradient with an Atom Interferometer-Based Gravity Gradiometer, *Phys. Rev. Lett.* **81**, 971 (1998).
- [23] C. J. Bordé, C. Salomon, S. Avrillier, A. van Lerberghe, C. Breant, D. Bassi, and G. Scoles, Optical Ramsey fringes with traveling waves, *Phys. Rev. A* **30**, 1836 (1984).
- [24] J. Olson, R. W. Fox, T. M. Fortier, T. F. Sheerin, R. C. Brown, H. Leopardi, R. E. Stoner, C. W. Oates, and A. D. Ludlow, Ramsey-Bordé Matter-Wave Interferometry for Laser Frequency Stabilization at 10^{-16} Frequency Instability and Below, *Phys. Rev. Lett.* **123**, 073202 (2019).
- [25] J. Keupp, A. Douillet, T. E. Mehlstäubler, N. Rehbein, E. M. Rasel, and W. Ertmer, A high-resolution Ramsey-Bordé spectrometer for optical clocks based on cold Mg atoms, *Eur. Phys. J. D* **36**, 289 (2005).
- [26] J. M. McGuirk, G. T. Foster, J. B. Fixler, M. J. Snadden, and M. A. Kasevich, Sensitive absolute-gravity gradiometry using atom interferometry, *Phys. Rev. A* **65**, 033608 (2002).
- [27] K. Chung, S. Chiow, S. Herrmann, S. Chu, and H. Müller, Atom interferometry tests of local Lorentz invariance in gravity and electrodynamics, *Phys. Rev. D* **80**, 016002 (2009).
- [28] E. Rocco, R. N. Palmer, T. Valenzuela, V. Boyer, A. Freise, and K. Bongs, Fluorescence detection at the atom shot noise limit for atom interferometry, *New J. Phys.* **16**, 093046 (2014).
- [29] M. Pappa, P. C. Condylis, G. O. Konstantinidis, V. Bolpasi, A. Lazoudis, O. Morizot, D. Sahagun, M. Baker, and W. von Klitzing, Ultra-sensitive atom imaging for matter-wave optics, *New J. Phys.* **13**, 115012 (2011).
- [30] P. J. Mohr, D. B. Newell, B. N. Taylor, and E. Tiesinga, Data and analysis for the CODATA 2017 special fundamental constants adjustment, *Metrologia* **55**, 125 (2018).
- [31] B. J. Mount, M. Redshaw, and E. G. Myers, Atomic masses of ${}^6\text{Li}$, ${}^{23}\text{Na}$, ${}^{39,41}\text{K}$, ${}^{85,87}\text{Rb}$, and ${}^{133}\text{Cs}$, *Phys. Rev. A* **82**, 042513 (2010).